1-1-2011

Self-assembly of [1010] grown ZnO nanowhiskers with exposed reactive (0001) facets on hollow spheres and their enhanced gas sensitivity

Jun Liu
junliu@uow.edu.au

Xiaolong Chen
Chinese Academy of Sciences Beijing

Wenjun Wang
Institute of Physics Chinese Academy of Sciences

Yu Liu
Chinese Academy of Sciences

Qingsong Huang
Chinese Academy of Sciences

See next page for additional authors

View Article Online / Journal Homepage / Table of Contents for this issue
Dynamic Article Links

CrystEngComm

Cite this: *CrystEngComm*, 2011, **13**, 3425

www.rsc.org/crystengcomm

PAPER

Self-assembly of [10$\bar{1}$0] grown ZnO nanowhiskers with exposed reactive (0001) facets on hollow spheres and their enhanced gas sensitivity†

Jun Liu,[ab] Xiaolong Chen,*[a] Wenjun Wang,[a] Yu Liu,[a] Qingsong Huang[a] and Zaiping Guo*[b]

Received 8th November 2010, Accepted 2nd February 2011
DOI: 10.1039/c0ce00821d

In this work, we demonstrate a simple gas-phase process to synthesize ZnO with exposed reactive {0001} facets without the use of any capping agent. The method is based on controlling the ZnO growth direction, causing it to switch from the typical [0001] to [10$\bar{1}$0], resulting in [10$\bar{1}$0] grown nanowhiskers with exposed reactive {0001} facets. Moreover, these nanowhiskers self-assemble on ZnO hollow spheres to form a three-dimensional hierarchical nanostructure, which stabilizes these nanowhiskers against agglomeration. Such a designed ZnO nanostructure endows the ZnO sensing material with both small crystal sizes and exposed reactive {0001} facets, which leads to greatly enhanced gas sensitivities compared to typical [0001] grown ZnO nanowires. Such reactive-facet-enhanced gas sensitivity is also shown by our calculation of the chemisorption energy of oxygen, based on density functional theory.

Introduction

As awareness of the need to protect the environment has grown and specific demands for industrial or domestic gas detection and monitoring have emerged, semiconductor gas sensors (SGS), known as chemoresistive gas sensors, which are typically based on metal oxides (*e.g.*, SnO_2, ZnO, In_2O_3, MoO_3, and V_2O_5), have received great attention.[1–6] In principle, gas sensing by metal-oxide semiconductors is based on the oxidation–reduction reaction of the detected gases occurring on the semiconductor surface, which leads to an abrupt change in the conductance of the sensor. For this reason, the sensitivity of SGS should depend on both the crystal sizes of the metal oxides and the surface atom structure of the exposed facets. The effective integration of small crystal sizes and favourable exposed reactive surfaces is also expected to be effective in promoting the chemical sorption of oxygen, thus enhancing gas sensitivity. However, such a strategy to improve the sensitivity of sensors has not attracted much attention up to now, possibly due to the difficulty of synthesizing metal-oxide nanocrystals with exposed reactive facets, which usually diminish rapidly during the crystal growth process as a result of the minimization of surface energy.[7] To the best of our knowledge, to date, only sub-micron SnO_2 single crystals with exposed high-index {221} facets have been reported to show improved sensitivity.[8] However, the gas sensitivity of such SnO_2 crystals has been intrinsically restricted by their relatively large crystal size (more than 100 nm) and by agglomeration of the crystal particles (leading to a correspondingly very small surface area). Therefore, it is still highly desirable to fabricate gas-sensing metal oxides with both small crystal size and exposed reactive facets, and then stabilize these as-synthesized nanocrystals against agglomeration to improve their gas sensitivity. The theory of reactive-facet-enhanced gas sensitivity is also worth studying.

Although there are a few reports on the syntheses of metal oxide crystals with reactive facets, these studies are mostly focused on a solution-phase process, in which capping agents are used to cap the reactive facets of the metal oxides to lower their surface energy and growth rate, so as to preserve the reactive facets during the growth process. For example, Yang *et al.* first developed hydrofluoric acid as a capping agent to successfully synthesize anatase TiO_2 single macro-crystals with a high percentage (47 per cent) of exposed reactive {001} facets *via* a solution-phase process.[9] Then, Mclaren *et al.* reported the synthesis of ZnO particles with exposed reactive {0001} facets by use of oleic acid as a capping agent and studied their enhanced photocatalytic activity.[10] In 2010, Yin *et al.* reported the synthesis of Fe_2O_3 single crystals with high-index reactive facets *via* a solution-phase process.[11] However, the capping agents that were used often involved extremely corrosive and toxic hydrofluoric acid or hydrochloric acid, which is against the principle of "green chemistry" and it is also reported that capping agents sometimes can passivate and destroy the reactive surfaces of the

[a]*Beijing National Laboratory for Condensed Matter Physics, Institute of Physics, Chinese Academy of Sciences, Beijing 100190, China. E-mail: chenx29@aphy.iphy.ac.cn; Fax: +86-010-82649646; Tel: +86-010-82649036*

[b]*Institute for Superconducting and Electronic Materials, University of Wollongong, NSW 2522. E-mail: zguo@uow.edu.au; Fax: +61 2 4221 5731; Tel: +61 2 4221 5225*

† Electronic supplementary information (ESI) available: SEM images of Zn products annealed for different times, experimental details for synthesis of ZnO nanobranches with typical [0001] grown nanowires, XRD pattern of ZnO nanobranches, SEM and TEM images of ZnO nanobranches, structural model of an oxygen molecule, total energy of each surface model of ZnO and chemisorption energy of O_2 molecule on each surface of ZnO. See DOI: 10.1039/c0ce00821d

metal oxides, which limits the reactivity of the reactive facets and their applications.[12] In terms of agent-free methods, there are few reports on the synthesis of metal oxides with reactive facets, except for the synthesis of TiO_2 particles with reactive {001} facets by a gas-phase reaction process with rapid heating and quenching.[13]

In this work, we demonstrate a simple gas-phase process to synthesize a metal oxide with exposed reactive facets at normal growth rates without the use of any capping agent. The work is based on changing the metal oxide growth direction from the preferred growth direction to another that will maintain the reactive facets. An attractive gas sensing material, ZnO, which has a strong preferential [0001] growth direction, which causes most synthesized ZnO nanostructures to have a very low percentage of exposed reactive {0001} facets,[14–17] has been selected as a specific example. We report a simple gas-phase synthesis process to control the ZnO growth direction, causing it to switch from the typical [0001] to [10$\bar{1}$0], resulting in [10$\bar{1}$0] grown nanowhiskers with exposed reactive {0001} facets. These nanowhiskers self-assemble on ZnO hollow spheres to form a three-dimensional hierarchical nanostructure, which stabilizes these nanowhiskers against agglomeration. In contrast to the solution route using capping agents, the present method simply uses single zinc crystals as both template and source to control the ZnO growth direction and synthesize ZnO with reactive facets *via* a gas-phase process, with no involvement of any capping agents. Such a designed hierarchical nanostructure endows the ZnO sensing material with both small crystal sizes and exposed reactive {0001} facets, which leads to greatly enhanced gas sensitivity compared to ZnO nanobranches with typical [0001] grown ZnO nanowires surrounded by low-energy {10$\bar{1}$0} facets. Such reactive-facet-enhanced gas sensitivity is also demonstrated by our calculation of the chemisorption energy of oxygen, based on density functional theory. Therefore, our work here not only achieves gas-sensing metal oxides with both small crystal sizes and a high proportion of reactive facets to greatly enhance their gas sensitivities, but also sheds new light on the synthesis of metal oxide nanostructures with exposed reactive facets by a gas-phase synthesis process without the use of any capping agent.

Experimental

The synthesis of [10$\bar{1}$0] grown ZnO nanowhisker arrays on ZnO hollow spheres consists of two steps, which were both performed in a horizontal tube furnace. Firstly, Zn powder (2 g, 99.99%), which had been loaded into an alumina boat, was placed in the central heating zone of a quartz tube in the furnace. The quartz tube was pumped and then filled with argon. After repeating the operation three times, the quartz tube was heated to 650 °C in 1/2 h under an argon flow of 100 standard cubic centimetres per minute (sccm) and normal pressure. After the quartz tube had been kept at this temperature for 5 min, it was suddenly cooled. Secondly, the products (Zn polyhedra and microspheres) at the end of the quartz tube were collected and put into the central heating zone of the quartz tube. In order to observe the detailed growth process, the quartz tube was heated to 300 °C in 20 min under oxygen atmosphere, and the annealing time was set from 5 min to more than 24 h at this temperature for different samples, with the annealing followed by rapid cooling. The products obtained with different annealing durations were examined and characterized.

Results and discussion

Fig. 1 shows the X-ray diffraction patterns (XRD) of the products in the first step and the samples annealed for different durations. The XRD pattern of the products in the first step can be well indexed to a hexagonal cell with $a = 2.664$ Å and $c = 4.946$ Å, in good agreement with the standard data (ICDD-PDF 65-5973), confirming that the products obtained in the first step are Zn with a hexagonal structure. The XRD pattern of the products annealed for more than 24 h can be well indexed to a hexagonal cell with $a = 3.244$ Å and $c = 5.198$ Å, in good agreement with the standard data (ICDD-PDF 36-1451), confirming that these products are ZnO with a hexagonal wurtzite structure. From the XRD patterns, it can be seen that the Zn products are gradually transformed to ZnO during annealing. The scanning electron microscope (SEM) image in Fig. 2(a) shows the large scale synthesis of products in the first step, which consist of Zn microspheres, 38-face polyhedra and icosahedra (Fig. 2(b–d)). The Zn microspheres are the main morphology. The transmission electron microscope (TEM) image and *in situ* electron diffraction pattern of a Zn icosahedron (Fig. 2(e)) indicate that the top and bottom surfaces of the icosahedra are {0001}, and the side surfaces are {10$\bar{1}$0}. According to the angle (about 45°) shown in the SEM images (Fig. 2(c) and (d)), the inclined surfaces could be {10$\bar{1}$1}. Therefore, the icosahedra are enclosed by {0001} (top and bottom surfaces), {10$\bar{1}$0} (side surfaces), and {10$\bar{1}$1} (inclined surfaces) facets. The 38-face polyhedra are enclosed by {0001} (top and bottom surfaces), {10$\bar{1}$0} (side surfaces), {10$\bar{1}$1} (inclined surfaces) and high index planes with rough surfaces. The same 38-face polyhedra were observed by Wang *et al.*[18]

The Zn icosahedra, 38-face polyhedra, and microspheres were then annealed at 300 °C for 5 min in an oxygen atmosphere, as shown in the TEM images in Fig. 3(a), (b) and (c), respectively. It can be seen that many white particles have emerged on the {0001}, {10$\bar{1}$0} and high index planes, but far fewer white particles have emerged on the {10$\bar{1}$1} surfaces. Moreover, it is

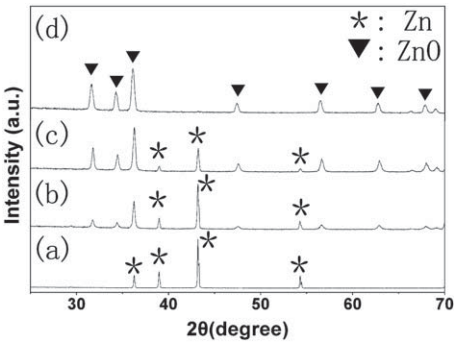

Fig. 1 XRD patterns of the products in the first step and after annealing for different durations: (a) the products obtained in the first step are single phase Zn, (b) Zn products annealed for one hour, (c) Zn products annealed for 5 h and (d) Zn products annealed for more than 24 h, with the pattern only showing ZnO single phase.

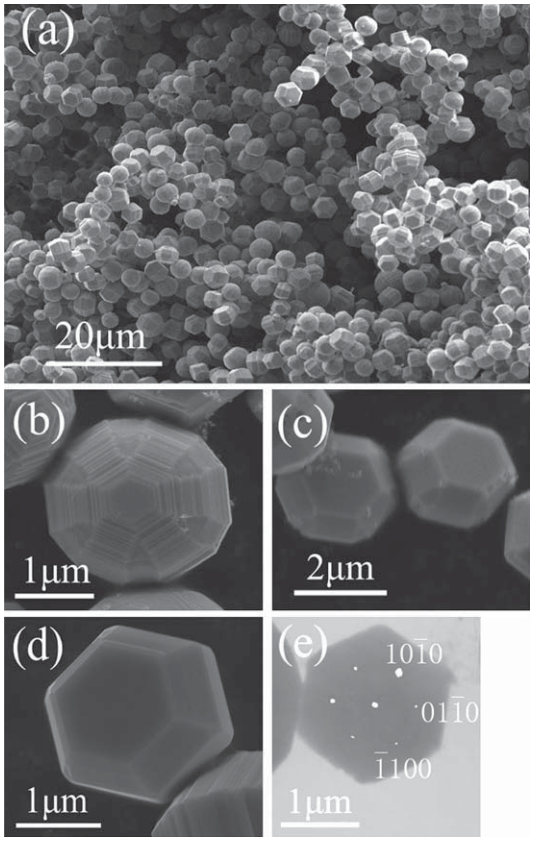

Fig. 2 SEM images of the Zn products obtained in the first step: (a) large-scale synthesis of Zn products, consisting of (b) Zn microspheres, (c) 38-face polyhedra and (d) icosahedra. (e) TEM image and *in situ* electron diffraction pattern of Zn icosahedron.

found that the white particles on the surfaces are nanoflakes, which are 20–30 nm in length and width and 2–5 nm thick, as shown in the inset image of Fig. 3(d). The flake nuclei on {0001} surfaces are at an angle of 60° or 120° to each other (Fig. 3(d)), but the flake nuclei on {10$\bar{1}$0} or high index planes are all parallel to each other (Fig. 3(e) and (f)).

Fig. 4(a) shows the morphology of the Zn microspheres annealed at 300 °C for 1 h. It can be seen that the flake nuclei on the side surfaces {10$\bar{1}$0} and high index planes grow longer and remain parallel to each other, while the flake nuclei on {0001} surfaces do not grow larger or longer and the {0001} surfaces become dented. With the Zn polyhedra and microspheres being further annealed at 300 °C for 5 h, the {0001} surfaces sank further and the polyhedron or microsphere centres all became concavo-concave microspheres. In the meanwhile, the flake nuclei on side surfaces {10$\bar{1}$0} and high index planes grew even longer and formed straight and thin nanowhiskers, as shown in Fig. 4(b).

For the Zn polyhedra and microspheres annealed at 300 °C for more than 24 h, the nanowhiskers on {10$\bar{1}$0} side surfaces and high index planes grew to be several tens of nanometres in thickness, several hundred nanometres in width and several microns in length, as shown in Fig. 5. The nanowhiskers, growing on six symmetrical high index planes, form a radial array in six-symmetry longitudinal planes. Moreover, the nanowhiskers growing on {10$\bar{1}$0} surfaces are at an angle of 60°

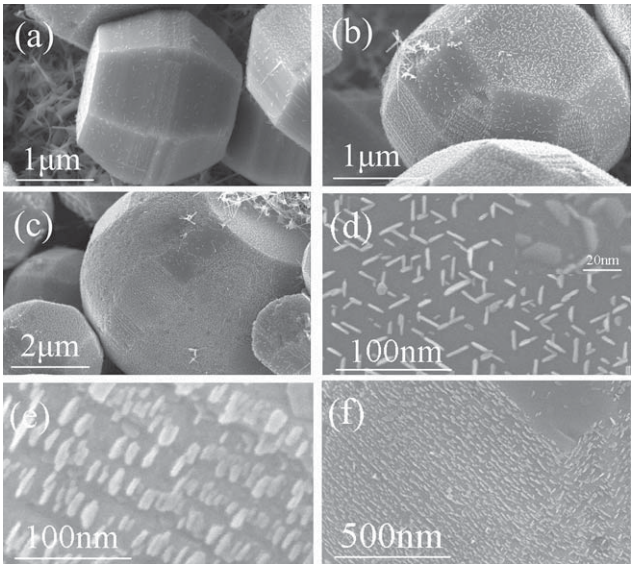

Fig. 3 SEM images of the Zn products annealed for 5 min:(a) nuclei on Zn icosahedra, (b) 38-face polyhedra and (c) microspheres. (d) Top view of the nuclei on {0001} surfaces, with the inset showing an enlarged SEM side-view image of the nuclei on a {0001} surface. This shows that the nuclei are all flake-like, with the flakes being about 20–30 nm in length and width and about 2–5 nm thick. These flake nuclei on {0001} surfaces are at an angle of 60° or 120° to each other. SEM images of the flake nuclei on (e) high index planes and (f) {10$\bar{1}$0} surfaces show that the flake nuclei on high index planes or {10$\bar{1}$0} are all parallel to each other.

to each other and form a parallel array in the equatorial plane (Fig. 5(b) and (c)). Enlarged SEM images of the top views and side views of such nanobelts are shown in the ESI in Fig. S1 and S2.† A TEM image of the whole hierarchical structure shows that the center concavo-concave microsphere is hollow (Fig. 6(a)). The high resolution transmission electron microscope (HRTEM) image and *in situ* electron diffraction pattern in Fig. 6(b) indicate that the ZnO nanowhiskers on {10$\bar{1}$0} surfaces and high index planes all grow along the *a* or *b* axis, not the typical *c* axis (a TEM image of a nanowhisker is shown in Fig. S3†). It is well known that ZnO in the hexagonal wurtzite structure can easily grow along the *c* axis to generate a hexagonal rod. This is because the (0001) facets have higher surface energy and a faster growth rate.[19] The specific surface area of the as-prepared sample of ZnO hierarchical nanostructures with [10$\bar{1}$0] grown nanowhisker arrays (designated as ZHNNA) was measured by the 15 point Brunauer-Emmett-Teller (BET) N_2 adsorption method. The as-prepared ZHNNA sample shows a high specific surface area (11.4 $m^2\ g^{-1}$).

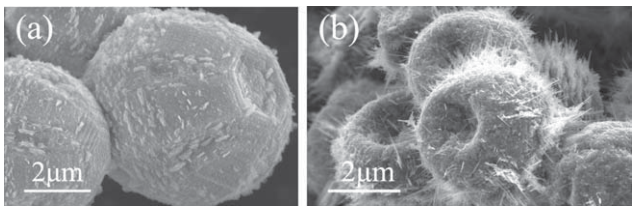

Fig. 4 SEM images of (a) the Zn products annealed for 1 h, (b) the Zn products annealed for 5 h.

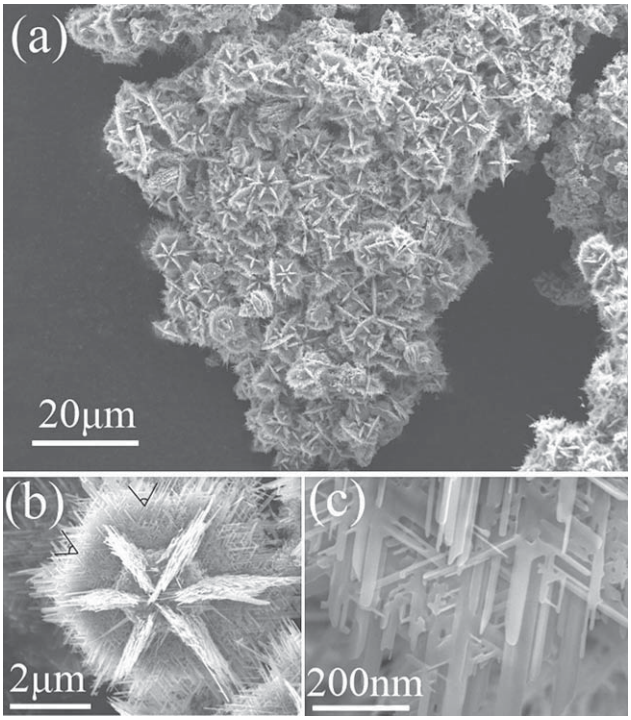

Fig. 5 SEM images of the Zn products annealed for more than 24 h: (a) annealing Zn polyhedra or microspheres can yield completely uniform hierarchical nanostructures, (b) top-view of a hierarchical nanostructure and (c) enlarged image of nanobelts of a hierarchical nanostructure.

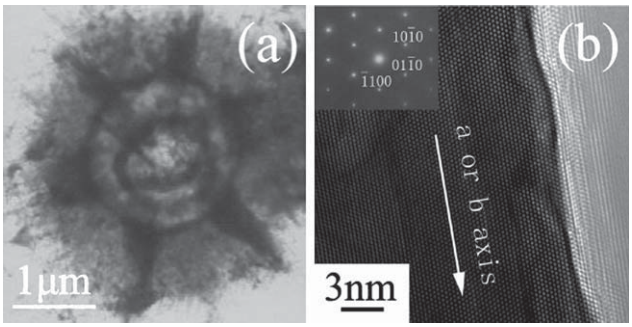

Fig. 6 (a) TEM image of a hierarchical nanostructure and (b) HRTEM image and *in situ* electron diffraction pattern (inset) show that the nanowhisker is a single crystal and grows along the *a* or *b* axis, not the typical *c* axis.

It is interesting to note that annealing both Zn polyhedra and Zn microspheres yields very uniform hierarchical nanostructures, in which [10$\bar{1}$0] grown ZnO nanowhiskers selectively and regularly self-assemble on concavo-concave microspheres. However, what is responsible for this effect and what controls the nucleation and growth process?

Based on experimental observations, a formation mechanism is proposed and illustrated in Scheme 1. The growth occurs at 300 °C, below the Zn melting point, and the Zn polyhedra and microspheres remain in the solid state, based on experimental observations, suggesting that the growth occurs *via* a solid-solid process. So, the solid Zn polyhedral and microsphere surfaces act as both reactants and substrates. To address how the Zn

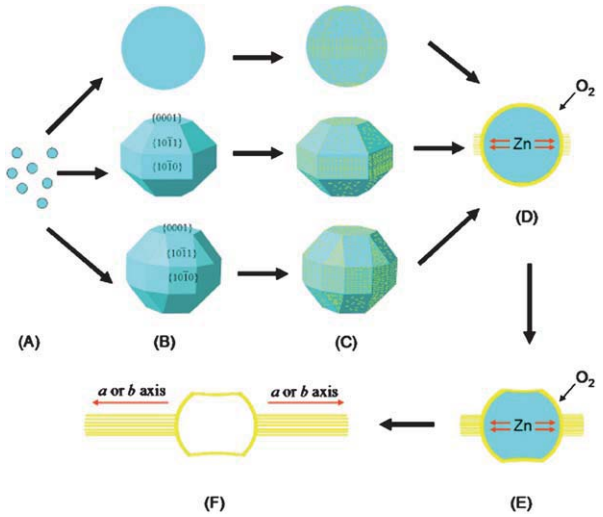

Scheme 1 Schematic illustration of "Kirkendall effect + anisotropic diffusion" process to form novel hollow ZnO nanostructure. In order to focus on the "Kirkendall effect + anisotropic diffusion" process, the nanobelts growing on the high index planes with rough surfaces are not discussed in the Scheme. (a) Zn vapor carried by the Ar gas, (b) the formation of a single Zn sphere, an icosahedron and a 38-face polyhedral crystal, (c) surface oxidation of the sphere and polyhedra to form regular ZnO flake nucleation (yellow colour) on each surface at 300 °C, (d) with extended oxidation time, the sphere and polyhedral surfaces form thin spherical ZnO layers (yellow colour), (e) due to anisotropic diffusion, the inner Zn atoms mainly out-diffuse along the *a* or *b* axis to react with the outer oxygen, which means that the flake nuclei on {0001} surfaces do not grow and the {0001} surfaces collapse, but the flakes on {10$\bar{1}$0} surfaces can grow longer and larger, (f) because the inner Zn atom out-diffusion rate is larger than the outer O atom in-diffusion rate, vacancy inward-diffusion will occur to compensate for the unequal material flow and eventually results in the formation of hollow structures (Kirkendall effect).

substrates affect the growth direction of ZnO and how ZnO selectively grows on the Zn polyhedra and microspheres, we compared the lattice mismatch of different interfaces between ZnO and Zn. For ZnO growing along the conventional preferential direction, [0001], on {10$\bar{1}$0} surfaces of the Zn crystal, the interface is composed of $\{0001\}_{ZnO}$ and $\{10\bar{1}0\}_{Zn}$. The corresponding lattice parameters can be determined as $a_{ZnO} = b_{ZnO} =$ 3.244 Å, and $a_{Zn} =$ 2.664 Å, $b_{Zn} =$ 4.947 Å. Thus, the lattice mismatch along the *a* direction is 22%, and the lattice mismatch along the *b* direction is 34%. Similarly, if ZnO grows along the [0001] direction on {0001} surfaces or on {10$\bar{1}$1} surfaces of a Zn crystal, the lattice mismatches along the *a* direction are both 22%, and the lattice mismatch along the *b* direction is 22% and 15.7%, respectively. For ZnO growing along the *a* or *b* axis on the {0001}, {10$\bar{1}$0} and {10$\bar{1}$1} surfaces of a Zn crystal, the lattice mismatches along the *a* direction are all 22%, while the lattice mismatch along the *b* direction is 2.3% (on Zn {0001} surfaces), 5.3% (on Zn {10$\bar{1}$0} surfaces) and 7% (on Zn {10$\bar{1}$1} surfaces), respectively. Therefore, the decreased lattice mismatch along the *b* direction should be responsible for the growth of the ZnO nanowhiskers along the *a* or *b* axis, not the typical *c* axis. This may also explain why the nuclei on the inclined {10$\bar{1}$1} surfaces are fewer than on the other surfaces, it is due to the larger lattice mismatch. This mechanism also applies to the Zn microspheres,

not only the Zn polyhedra, because the Zn microspheres are single crystals with the same inner atomic arrays as the Zn polyhedra. The Zn microsphere poles are {0001} facets with a hexagonal shape and the equators of the Zn microspheres have the same atomic arrays as the $\{10\bar{1}0\}$ facets that form the equatorial planes of the Zn polyhedra.

In the initial growth stage, as ZnO has a larger surface energy than the Zn substrate, because the binding energy between Zn and O is stronger than that between Zn and Zn and there are large lattice mismatches between the Zn substrate and ZnO, isolated island nuclei (Volmer-Weber (V-W) mode) are favoured (Scheme 1(c)). The mechanism behind the development of the island nuclei into two-dimensional flakes and their self-assembly in a regular manner on Zn polyhedral and microsphere surfaces are possibly determined by Zn atom anisotropic diffusion on different surfaces of Zn polyhedra and microspheres. Similar anisotropic surface diffusion is also observed in vapour deposition[20–22] and has been analyzed.[23]

During further growth, the density of flakes becomes higher. Neighbouring flakes will compete for the diffusing Zn atoms on surfaces, which results in a decrease in the ZnO flake growth rate. At a certain ZnO flake concentration threshold, the Zn atoms on surfaces of Zn polyhedra or microspheres will gradually react with oxygen to form thin ZnO spherical walls, a process which is driven by the decrease in surface energy (Scheme 1(d)). Once the thin ZnO spherical walls are formed, the inner Zn atoms can only out-diffuse through the ZnO wall to react with oxygen, which is driven by the concentration gradient and the Gibbs-Thomson effect (Scheme 1(e)). At the same time, the outer O atoms will in-diffuse to react with Zn atoms. Because the diffusion rate of the inner Zn is larger than that of the O atoms, vacancy inward-diffusion will occur to compensate for the unequal material flow and this eventually results in the formation of hollow structures. (Scheme 1(f)). This non-equilibrium mutual diffusion process is based on the Kirkendall effect,[24] a classical phenomenon in metallurgy. In recent years, since Alivisatos *et al.* developed an interesting method, based on the Kirkendall effect, to synthesize CoO hollow spheres,[25] the Kirkendall effect, as an effective template-free method, has been widely applied for the fabrication of various hollow structures.[26–31] The basis of the Kirkendall effect is void formation caused by the difference in diffusion rates between two species. The conventional treatment of this process only considers the bulk diffusion of growth species and vacancies.[32] Recently, Fan *et al.* proposed that surface diffusion *via* the interior pore surfaces played an important role in the formation of hollow structures by the Kirkendall effect.[33] The bulk and surface diffusions in the Kirkendall process considered so far are assumed to be isotropic, which leads to the formation of hollow structures, such as hollow spheres or hollow tubes. However, as a matter of fact, the two types of diffusion are often anisotropic for a single crystal core. In the case of hexagonal Zn single crystals, Shirn at al. reported that the Zn atom self-diffusion rate along the *a* or *b* axis at 268 °C is as much as 4.5 times higher than the Zn atom self-diffusion rate along the *c* axis at 374 °C.[34] Our experiments also show that Zn atom out-diffusion along the *a* or *b* axis is much easier than along the *c* axis. This is the reason why the flakes on $\{10\bar{1}0\}$ surfaces grow longer and larger due to the abundant Zn supply. This is also why the flake nuclei on {0001} surfaces do not grow larger and the {0001} surfaces collapse, but the flakes on $\{10\bar{1}0\}$ surfaces can grow longer and larger, although there are flakes on both {0001} and $\{10\bar{1}0\}$ surfaces in the nucleation process. So, the anisotropic diffusion plays an important role in the further growth process, which controls inner atom transport to selectively support the growth of surface flakes. The formation of the novel ZnO hollow nanostructure is possibly based on a "Kirkendall effect + anisotropic diffusion" process (as shown in Scheme 1). Note that in order to focus on the "Kirkendall effect + anisotropic diffusion" process, the nanowhiskers growing on the high index planes with rough surfaces are not discussed in Scheme 1.

Fig. 7 presents a comparison of the response/recovery time of a ZHNNA sample and of ZnO nanobranches with typical [0001] grown nanowires, on exposure to 100 ppm of ethanol at 260 °C. ZnO nanobranches with uniform [0001] grown nanowires are largely synthesized by a vapor-solid method (the experimental details, XRD patterns and SEM and TEM images are shown in Fig. S4, S5 and S6†). It is obvious that the ZHNNA exhibit a much higher gas response than that of the ZnO nanobranches with typical [0001] grown nanowires. The magnitude of the gas sensitivity is estimated to be 10.9 and 2.4 for the ZHNNA and ZnO nanobranches, respectively. The response time, T_{des} (defined as the time required for the resistance to change from R_0 to $R_0 - 90\%(R_0 - R_x)$, where R_0 is the unexposed resistance and R_x is the resistance at greatest response), for ZHNNA (45 s) is similar to that of the ZnO nanobranches (37 s). However, ZHNNA show a faster recovery time, T_{rev} (defined as the time required for the resistance to change from R_x to $R_x + (R_0 - R_x)/e$), this is 6 s for ZHNNA and 15 s for the ZnO nanobranches, respectively. The improvement of the sensing properties is further demonstrated in the sensitivity *vs.* concentration curve presented in Fig. 8. The gas response of ZHNNA is 3 times higher, on average, than that of the ZnO nanobranches with typical [0001] grown nanowires.

It was reported recently that ZnO nanodisks with (0001) facets are chemically more reactive than those with $(10\bar{1}0)$ facets, based

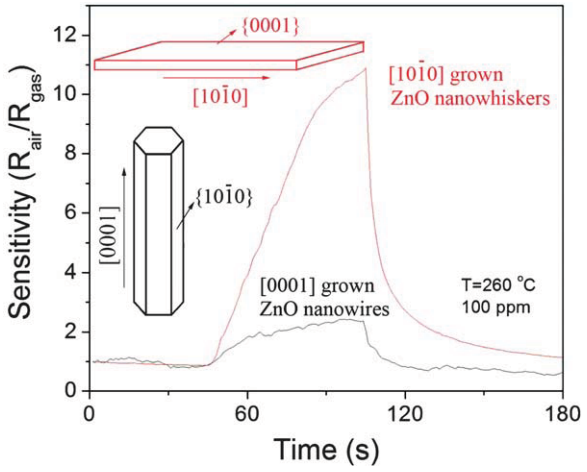

Fig. 7 A comparison between $[10\bar{1}0]$ grown ZnO nanowhisker arrays and typical [0001] grown ZnO nanowires of their sensitivity to 100 ppm of ethanol gas at 260 °C. The insets are models for a single $[10\bar{1}0]$ grown ZnO nanowhisker with exposed reactive {0001} facets (red) and a single [0001] grown ZnO nanowire surrounded by low-energy side $\{10\bar{1}0\}$ surfaces (black).

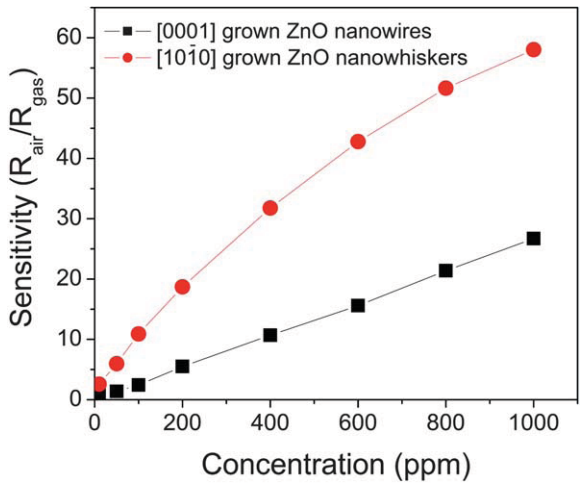

Fig. 8 The gas response of [10$\bar{1}$0] grown ZnO nanowhisker arrays and [0001] grown ZnO nanowires towards different concentrations of ethanol gas at 260 °C.

on experimental results.[35,36] However, the fundamental question of how this happens has not been answered. To clarify this, we calculated the chemisorption energy of an oxygen molecule (O_2) on different facets of ZnO by density functional theory. The O_2 molecule model is shown in S7.† The models of ZnO for each surface and each surface with an oxygen molecule added are all slab models ($3 \times 3 \times 2$), as shown in Fig. S8† and Fig. 9. All calculations have been carried out using density functional theory (DFT) within the generalized-gradient approximation (GGA) using the Perdew–Burke–Ernzerhof (PBE) potential function,[37] based on the ultrasoft pseudopotential method.[38,39] This has been implemented in the CASTEP package.[40] The CASTEP calculation is performed on superlattices, which consist of identical films separated by thick (≥10 Å) vacuum layers. The geometric structures of all the models are optimized using the Broyden-Fletcher-Goldfarb-Shanno (BFGS) minimizer in the CASTEP package with default convergence tolerances: 5.0×10^{-6} eV/atom for energy, 0.01 eV Å^{-1} for maximum force and 5.0×10^{-4} Å for maximum displacement. The other parameters of the band structure calculation are as follows: the energy cut-off for the plane wave basis set is 380 eV, k-points are generated according to the Monkhorst–Pack grid with separations of 0.04 Å^{-1} and the energy tolerance for self-consistency is 5.0×10^{-7} eV/atom. Our calculations show that the reduced energy is 1.16 eV when the O_2 molecule is chemically absorbed on the (0001) facet, however, if the O_2 molecule is chemically absorbed on the (10$\bar{1}$0) or (10$\bar{1}$1) facets then the reduced energies are 0.14 eV and −0.1 eV, respectively (as shown in Table 1). The higher the reduced energy is, the easier the chemisorption of oxygen becomes. That is to say, it is easier for the reactive (0001) facet to chemically absorb O_2 molecules than it is for the other facets under the same conditions. The greater the amount of chemically-absorbed oxygen on the surface there is, the stronger the chemical reactivity of the surface becomes.[41]

It is well accepted that the gas response of semiconductor gas sensors is attributable to the chemical absorption of oxygen on the oxide surface and the subsequent reaction between adsorbed oxygen and the test gas, which brings about a resistance change. For ZnO nanomaterials in ethanol gas sensing, oxygen is adsorbed on the exposed surface of the ZnO, captures electrons from the conduction band, and ionizes to O^- or O^{2-}.[36] As a result, a depletion layer is formed on the surface of the ZnO, resulting in a decrease in the carrier concentration and the electron mobility. When the sensor is exposed to a reducing gas such as ethanol gas, the reducing gas may react with the adsorbed oxygen molecule and release the trapped electrons back to the conduction band, thereby increasing the carrier concentration

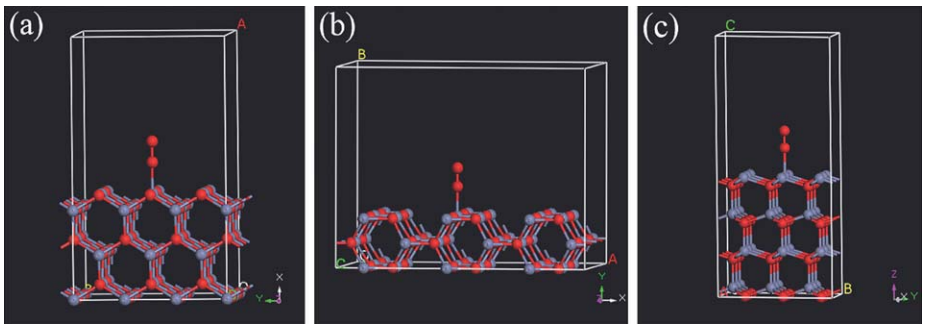

Fig. 9 Slab models of ZnO (a) (10$\bar{1}$0), (b) (10$\bar{1}$1) and (c) (0001) surfaces with an oxygen molecule added.

Table 1 Calculation for each model of the total energy and chemisorption energy[a] of an O_2 molecule on each surface of ZnO

(0001) facet simulation	Total energy (eV)	(10$\bar{1}$0) facet simulation	Total energy (eV)	(10$\bar{1}$1) facet simulation	Total energy (eV)
O_2 molecule	−867.96	O_2 molecule	−867.96	O_2 molecule	−867.96
ZnO (0001)	−77 285.37	ZnO (10$\bar{1}$0)	−77288.2	ZnO (10$\bar{1}$1)	−77276.84
ZnO (0001) added O_2	−78 154.49	ZnO (10$\bar{1}$0) added O_2	−78156.3	ZnO (10$\bar{1}$1) added O_2	−78144.70
ΔE_{chem}	−1.16 eV	ΔE_{chem}	−0.14 eV	ΔE_{chem}	0.10 eV

[a] Chemisorption energy, ΔE_{chem}, is defined as $\Delta E_{chem} = E_{O_2 \text{ molecule on surface}} - E_{surface} - E_{O_2 \text{ molecule}}$

and carrier mobility of ZnO. This eventually increases the conductivity of ZnO, as described in eqn (1) and (2):

$$C_2H_5OH + 6O^- \rightarrow 2CO_2 + 3H_2O + 6e^- \quad (1)$$

$$C_2H_5OH + 6O^{2-} \rightarrow 2CO_2 + 3H_2O + 12e^- \quad (2)$$

It is obvious that the sensitivity is greatly dependent on the amount of chemisorbed oxygen. In the case of ZnO, it is easier for the reactive (0001) facet to chemically absorb O_2 molecules than it is for the other facets. In the same ethanol vapor at the same concentration, the reactive (0001) facet will chemically absorb a greater amount of oxygen than the other facets. That is why ZHNNA with exposed reactive (0001) facets show greatly enhanced gas sensitivity compared to ZnO nanobranches with typical [0001] grown nanowires surrounded by $\{10\bar{1}0\}$ surfaces.

Conclusion

In conclusion, we demonstrate a simple gas-phase synthesis process to successfully synthesize $[10\bar{1}0]$ grown ZnO nanowhiskers with exposed reactive {0001} facets, which are self-assembled into a three-dimensional hierarchical nanostructure, stabilizing these nanowhiskers against agglomeration. To the best of our knowledge, this is the first time that $[10\bar{1}0]$ grown ZnO nanowhisker arrays self-assembled on a hollow sphere have been synthesized. Such a designed nanostructure endows the ZnO sensing materials with both small crystal sizes and exposed reactive {0001} facets, giving them greatly enhanced ethanol sensing properties compared to typical [0001] grown ZnO nanowires, with $\{10\bar{1}0\}$ side surfaces. Such reactive-facet-enhanced gas sensitivity is also shown by our calculation of the chemisorption energy of oxygen, based on density functional theory. Therefore, our work here not only achieves gas-sensing metal oxides with both small crystal sizes and high reactive facets to greatly enhance their gas sensitivities, but also sheds new light on the synthesis of metal oxide nanostructures with exposed reactive facets by a gas-phase synthesis process, without the use of any capping agent.

Notes and references

1 J. Du, D. Liang, H. Tang and X. Gao, *Nano Lett.*, 2009, **9**, 4348–4351.
2 N. Du, H. Zhang, B. D. Chen, X. Y. Ma, Z. H. Liu, J. B. Wu and D. R. Yang, *Adv. Mater.*, 2007, **19**, 1641.
3 Y. M. Wang, G. J. Du, H. Liu, D. Liu, S. B. Qin, N. Wang, C. G. Hu, X. T. Tao, J. Jiao, J. Y. Wang and Z. L. Wang, *Adv. Funct. Mater.*, 2008, **18**, 1131–1137.
4 A. Kolmakov, D. O. Klenov, Y. Lilach, S. Stemmer and M. Moskovits, *Nano Lett.*, 2005, **5**, 667–673.
5 X. D. Wang, C. J. Summers and Z. L. Wang, *Nano Lett.*, 2004, **4**, 423–426.
6 J. Liu, X. L. Chen, W. J. Wang, B. Song and Q. S. Huang, *Cryst. Growth Des.*, 2009, **9**, 1757.
7 T. L. Sounart, J. Liu, J. A. Voigt, M. Huo, E. D. Spoerke and B. Mckenzie, *J. Am. Chem. Soc.*, 2007, **129**, 15786–15793.
8 X. G. Han, M. S. Jin, S. F. Xie, Q. Kuang, Z. Y. Jiang, Y. Q. Jiang, Z. X. Xie and L. S. Zhang, *Angew. Chem., Int. Ed.*, 2009, **48**, 9180–9183.
9 H. G. Yang, C. H. Sun, S. Z. Qiao, J. Zou, G. Liu, S. C. Smith, H. M. Cheng and G. Q. Lu, *Nature*, 2008, **453**, 638–642.
10 A. Mclaren, T. Valdes-Solis, G. Q. Li and S. C. Tsang, *J. Am. Chem. Soc.*, 2009, **131**, 12540–12541.
11 J. Z. Yin, Z. N. Yu, F. Gao, J. J. Wang, H. Pang and Q. Y. Lu, *Angew. Chem., Int. Ed.*, 2010, **49**, 6328–6332.
12 H. G. Yang, G. Liu, S. Z. Qiao, C. H. Sun, Y. G. Jin, S. C. Smith, J. Zou, H. M. Cheng and G. Q. Lu, *J. Am. Chem. Soc.*, 2009, **131**, 4078.
13 F. Amano, O. Prieto-Mahaney, Y. Terada, T. Yasumato, T. Shibayama and B. Ohtani, *Chem. Mater.*, 2009, **21**, 2601–2603.
14 M. H. Huang, S. Mao, H. Feick, H. Q. Yan, Y. Y. Wu, H. Kind, E. Weber, R. Russo and P. D. Yang, *Science*, 2001, **292**, 1897–1899.
15 Y. Qin, X. D. Wang and Z. L. Wang, *Nature*, 2008, **451**, 809.
16 J. Y. Li, X. L. Chen, H. Li, M. He and Z. Y. Qiao, *J. Cryst. Growth*, 2001, **233**, 5–7.
17 L. Dai, X. L. Chen, X. N. Zhang, A. Z. Jin, T. Zhou, B. Q. Hu and Z. Zhang, *J. Appl. Phys.*, 2002, **92**, 1062–1064.
18 P. X. Gao and Z. L. Wang, *J. Am. Chem. Soc.*, 2003, **125**, 11299.
19 X. D. Wang, J. H. Song, P. Li, J. H. Ryou, R. D. Dupuis, C. J. Summers and Z. L. Wang, *J. Am. Chem. Soc.*, 2005, **127**, 7920–7923.
20 J. Abel, D. J. Kim, E. A. Everett and H. Yang, *J. Cryst. Growth*, 2008, **310**, 2244.
21 I. V. Shvets, S. Murphy and V. Kalinin, *Surf. Sci.*, 2007, **601**, 3169.
22 D. J. Kim, E. A. Everett and H. Yang, *J. Appl. Phys.*, 2007, **101**, 106106.
23 Y. X. Wang, Z. Y. Pan, T. J. Liu, X. M. Jiang, L. Zhou and J. Zhu, *Appl. Surf. Sci.*, 2006, **253**, 1748.
24 P. M. F. J. Costa, T. W. Hansen, J. B. Wagner and R. E. Dunin-Borkowski, *Chem.–Eur. J.*, 2010, **16**, 11809–11812.
25 Y. D. Yin, R. M. Rioux, C. K. Erdonmez, S. Hughes, G. A. Somorjai and A. P. Alivisatos, *Science*, 2004, **304**, 711.
26 H. J. Fan, M. Knez, R. Scholz, D. Hesse, K. Nielsch, M. Zacharias and U. Gösele, *Nano Lett.*, 2007, **7**, 993.
27 A. Cabot, R. K. Smith, Y. D. Yin, H. M. Zheng, B. M. Reinhard, H. T. Liu and A. P. Alivisatos, *ACS Nano*, 2008, **2**, 1452.
28 J. H. Gao, B. Zhang, X. X. Zhang and B. Xu, *Angew. Chem., Int. Ed.*, 2006, **45**, 1220.
29 Y. D. Yin, C. K. Erdonmez, A. Cabot, S. Hughes and A. P. Alivisatos, *Adv. Funct. Mater.*, 2006, **16**, 1389.
30 B. Liu and H. C. Zeng, *J. Am. Chem. Soc.*, 2004, **126**, 16744.
31 J. Liu, W. J. Wang, Z. P. Guo, R. Zeng, S. X. Dou and X. L. Chen, *Chem. Commun.*, 2010, **46**, 3887–3889.
32 K. N. Tu and U. Gösele, *Appl. Phys. Lett.*, 2005, **86**, 093111.
33 H. J. Fan, M. Knez, R. Scholz, D. Hesse, K. Nielsch, M. Zacharias and U. Gösele, *Nano Lett.*, 2007, **7**, 993.
34 G. A. Shirn, E. S. Wajda and H. B. Huntington, *Acta Metall.*, 1953, **1**, 513.
35 J. H. Zeng, B. B. Jin and Y. F. Wang, *Chem. Phys. Lett.*, 2009, **472**, 90–95.
36 A. Mclaren, T. Valdes-Solis, G. Q. Li and S. C. Tsang, *J. Am. Chem. Soc.*, 2009, **131**, 12540–12541.
37 J. P. Perdew, K. Burke and M. Ernzerhof, *Phys. Rev. Lett.*, 1996, **77**, 3865.
38 D. R. Hamann, M. Schluter and C. Chiang, *Phys. Rev. Lett.*, 1979, **43**, 1494.
39 D. Vanderbilt, *Phys. Rev. B: Condens. Matter*, 1990, **41**, 7892.
40 M. D. Segall, P. J. D. Lindan, M. J. Probert, C. J. Pickard, P. J. Hasnip, S. J. Clark and M. C. Payne, *J. Phys.: Condens. Matter*, 2002, **14**, 2717.
41 H. Windischmann and P. J. Mark, *J. Electrochem. Soc.*, 1979, **126**, 627.